



Nonstationary Fast-driven, Self-organized Criticality in Solar Flares

Markus J. Aschwanden 

Solar and Astrophysics Laboratory, Lockheed Martin Advanced Technology Center, Dept. ADBS, Bldg. 252, 3251 Hanover St., Palo Alto, CA 94304, USA
aschwanden@lmsal.com

Received 2019 September 17; revised 2019 October 31; accepted 2019 October 31; published 2019 December 11

Abstract

The original concept of self-organized criticality, applied to solar flare statistics, assumed a slow-driven and stationary flaring rate, which implies timescale separation (between flare durations and interflare waiting times). The concept reproduces power-law distributions for flare peak fluxes and durations, but predicts an exponential waiting time distribution. In contrast to these classical assumptions, we observe (i) multiple energy dissipation episodes during most flares, (ii) violation of the principle of timescale separation, (iii) a fast-driven and nonstationary flaring rate, (iv) a power-law distribution for waiting times Δt , with a slope of $\alpha_{\Delta t} \approx 2.0$, as predicted from the universal reciprocity between mean flaring rates and mean waiting times, and (v) pulses with rise times and decay times of the dissipated magnetic free energy on timescales of 12 ± 6 minutes, and up to 13 times in long-duration ($\lesssim 4$ hr) flares. These results are inconsistent with coronal long-term energy storage, but require photospheric–chromospheric current injections into the corona.

Unified Astronomy Thesaurus concepts: [Solar corona \(1483\)](#); [Solar magnetic fields \(1503\)](#); [Solar flares \(1496\)](#)

1. Introduction

Self-organized criticality (SOC) models are extremely useful to obtain physical scaling laws from the statistics of nonlinear energy dissipation processes (for reviews, see Charbonneau et al. 2001; Aschwanden 2011a, 2019a; Pruessner 2012; Charbonneau 2013; Aschwanden et al. 2016a, and references therein). The original concept of avalanches that occur randomly above some threshold, triggered by continuously dripped sand grains on top of a sandpile in a critical state, is due to Bak et al. (1987), while the first applications to solar flare statistics were explored by Lu & Hamilton (1991) and Crosby et al. (1993). SOC models can be tested by the power-law distributions of various geometric, temporal, and other physical parameters, which should reveal power-law slopes that are consistent with the underlying physical scaling laws, as well as with the functional shape of their waiting time distributions. In a slow-driven SOC model, avalanches occur rarely and are temporally separated, a condition that is called timescale separation, where the avalanche duration is smaller than the waiting time ($\tau_{\text{flare}} < \tau_{\text{wait}}$). This inequality is reversed in fast-driven SOC systems by definition, i.e., $\tau_{\text{flare}} > \tau_{\text{wait}}$. In this study, we will demonstrate that the timescale separation is often violated in the case of solar flares. While the energy build-up or storage time is much longer than the duration of an avalanche in a classical slow-driven SOC system (Figure 1(a)), we find here that the energy build-up or storage time is comparable with the energy dissipation time (of free magnetic energy), being a fraction of the flare duration only (Figure 1(b)), and thus much shorter than the waiting time between two subsequent flares.

This new aspect of fast-driven SOC systems has some far-reaching consequences that have virtually not been investigated yet. The power-law slope of flare durations, which typically has a value of $\alpha_T \approx 2.0$, revealed higher values of $\alpha_T \approx 2.0$ –5.0 during solar cycle maximum years, which was interpreted as a solar-cycle-dependent flare pile-up bias (Aschwanden 2011a, 2011b, 2011c; Aschwanden & Freeland 2012). Sufficiently fast-driven sandpile models produce frequent occurrences,

where many avalanches mutually overlap in time, and identification and definition of single events become problematic due to the violation of timescale separation. This temporal overlap problem is particularly problematic for one-dimensional data (such as light curves of flares at a given wavelength), but is much alleviated in two-dimensional data (where near-simultaneous events can be separated in space and time).

Another test bed of fast-driven SOC models is the waiting time (or interflare time interval) distribution. In classical slow-driven sandpile SOC models, individual avalanches occur independently of each other, which predicts an exponential (Poissonian) waiting time distribution for stationary flaring rates. However, nonstationary flaring rates produce different waiting time distributions, which depend on the variability function of the flaring rate (Wheatland et al. 1998; Wheatland 2000c, 2002, 2006). In this study, we emphasize the novel model of the Poissonian nonstationary waiting time distribution that is based on the universal reciprocity of flaring rates and mean flare waiting times (Aschwanden & McTiernan 2010). This universal model has no free parameters (except for a normalization constant) and predicts a power-law slope of $\alpha_{\Delta t} = 2$, which mostly agrees with the observations of solar flares (Wheatland et al. 1998; Moon et al. 2001; Wheatland 2003; Aschwanden & McTiernan 2010; Kanazir & Wheatland 2010).

The goal of this study is to gain a deeper understanding of nonstandard SOC models applied to solar flares, addressing slow-driven versus fast-driven SOC models, the timescale separation, the multiplicity of energy-release pulses during a single avalanche event, the violation of timescale separation, and the universal Poissonian nonstationary waiting time distribution. For this purpose, we use Helioseismic and Magnetic Imager (HMI)/*Solar Dynamics Observatory* (SDO) two-dimensional images for the analysis, which allows the free magnetic energy released for each time step during the solar flare to be computed. We present a brief description of both the analytical and numerical theory of waiting time distributions (Section 2), observations and data analysis of solar flare data

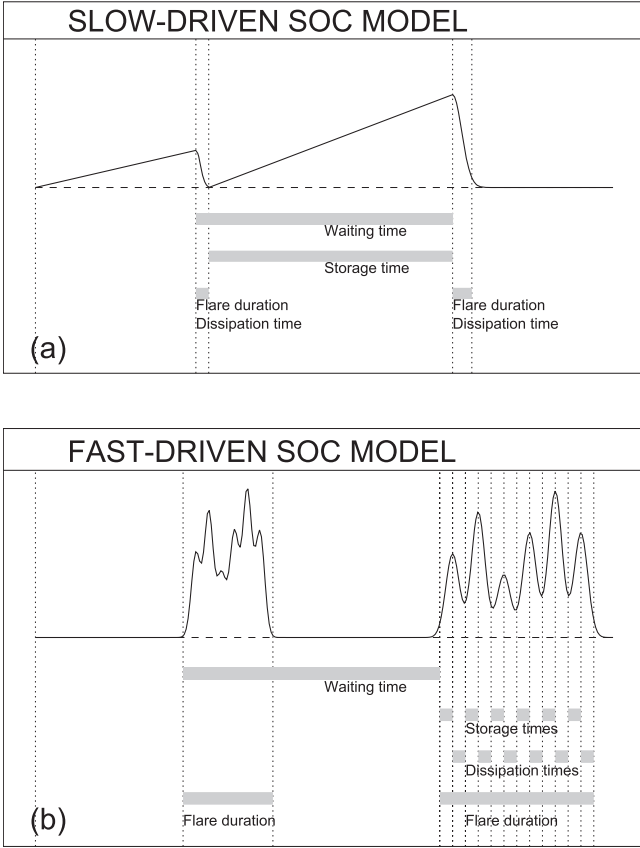


Figure 1. Definition of timescales for the slow-driven SOC model, according to the Rosner & Vaiana (1978) model (top panel), and the fast-driven SOC model proposed in this study (bottom panel). The x -axis represents the time, and the y -axis represents the time evolution of the free energy $E_{\text{free}}(t)$ that is dissipated during flares.

used and magnetic field computations (Section 3), a discussion of the new findings (Section 4), and conclusions (Section 5).

2. Theory

2.1. Analytical Waiting Time Distribution

Waiting times Δt , the inter-event time intervals between two subsequent events of a Poissonian point process, are expected to exhibit an exponential function in the case of a stationary random process. The time series sample may consist of time intervals observed in statistically independent events and sampled at different locations and times. Thus, the probability distribution function $p(\Delta t)$ is defined by

$$p(\Delta t) = \lambda_0 \exp^{-\lambda_0 \Delta t}, \quad (1)$$

where λ_0 represents the mean event occurrence rate and the distribution is normalized to unity, i.e., $\int_0^\infty p(\Delta t) d\Delta t = 1$. A random process can be called a stationary Poisson process when the average flaring rate λ_0 is time independent and stays constant as a function of time.

A more general approach of waiting time distributions is the concept of inhomogeneous or nonstationary Poisson processes, where the mean flaring rate $\lambda(t)$ becomes a function of time itself (e.g., Scargle 1998; Wheatland et al. 1998, 2000; Litvinenko & Wheatland 2001; Wheatland & Litvinenko 2002; Jaynes 2003; Sivia & Skilling 2006). Applying Bayesian statistics, a time series can be subdivided into Bayesian blocks,

during which the occurrence rate λ_i is assumed to be piecewise stationary during a time interval $[t_i, t_{i+1}]$,

$$p(t, \Delta t) = \begin{cases} \lambda_1 \exp^{-\lambda_1 \Delta t} & \text{for } t_1 < t < t_2 \\ \lambda_2 \exp^{-\lambda_2 \Delta t} & \text{for } t_2 < t < t_3 \\ \dots\dots\dots \\ \lambda_n \exp^{-\lambda_n \Delta t} & \text{for } t_n < t < t_{n+1} \end{cases} \quad (2)$$

The summation of the piecewise Bayesian blocks over discrete time intervals can be converted into a continuous integral function,

$$p(\Delta t) = \int_0^T \lambda(t) p(t, \Delta t) dt, \quad (3)$$

where the probability $p(t, \Delta t)$ in each Bayesian block is weighted by the number of events $\lambda(t)$. The total duration of the time series is T , and the normalization is given by the total number of events, i.e., $N = \int_0^T \lambda(t) dt$. Inserting the time-dependent probability $p(t, \Delta t) = \lambda(t) \exp^{-\lambda(t) \Delta t}$ into Equation (3) yields

$$p(\Delta t) = \frac{\int_0^T \lambda(t)^2 \exp^{-\lambda(t) \Delta t} dt}{\int_0^T \lambda(t) dt}. \quad (4)$$

Following Wheatland et al. (1998, 2000), we substitute the time variable t with the event occurrence rate λ , by defining the function $f(\lambda) = (1/T) dt(\lambda)/d\lambda$, which is equivalent to $f(\lambda) d\lambda = dt/T$,

$$p(\Delta t) = \frac{\int_0^\infty f(\lambda) \lambda^2 \exp^{-\lambda \Delta t} d\lambda}{\int_0^\infty \lambda f(\lambda) d\lambda}. \quad (5)$$

We now make a special choice for the flaring rate distribution $f(\lambda)$ that contains (i) a reciprocal relationship $f(\lambda) \propto \lambda^{-1}$ for small flaring rates $\lambda \lesssim \lambda_0$ and (ii) contains an exponential drop-off at large flaring rates $\lambda \gtrsim \lambda_0$ (see also Equation 5.2.16 in Aschwanden 2011a),

$$f(\lambda) = \lambda^{-1} \exp\left(-\frac{\lambda}{\lambda_0}\right). \quad (6)$$

The scale-free range of $\lambda < \lambda_0$ is visualized in Figure 2 (left panel, solid line), together with the exponential component (Figure 2, left panel, dashed line). The scale-free property with the scaling $f(\lambda) \propto \lambda^{-1}$ is easy to understand, because the number of events $f(\lambda)$ is proportional to the mean waiting time $\langle \Delta t \rangle$, which in turn is reciprocal to the mean flaring rate $\langle \lambda \rangle$, e.g., $f(\lambda) \propto \langle \lambda^{-1} \rangle \propto \langle \Delta t \rangle$, and thus is universally valid for every waiting time distribution. In addition, the exponential term in Equation (6) essentially produces an upper boundary of the reciprocal function at $\lambda \gtrsim \lambda_0$. The expression given in Equation (6) also fulfills the normalization $\int_0^\infty \lambda f(\lambda) d\lambda = \lambda_0$. The waiting time distribution (Equation (5)) can then be written as

$$p(\Delta t) = \int_0^\infty \left(\frac{\lambda}{\lambda_0}\right) \exp\left(-\frac{\lambda}{\lambda_0} [1 + \lambda_0 \Delta t]\right) d\lambda, \quad (7)$$

which, by defining $a = -(1 + \lambda_0 \Delta t)/\lambda_0$, corresponds to the integral $\int x e^{ax} dx = (e^{ax}/a^2)(ax - 1)$ and becomes

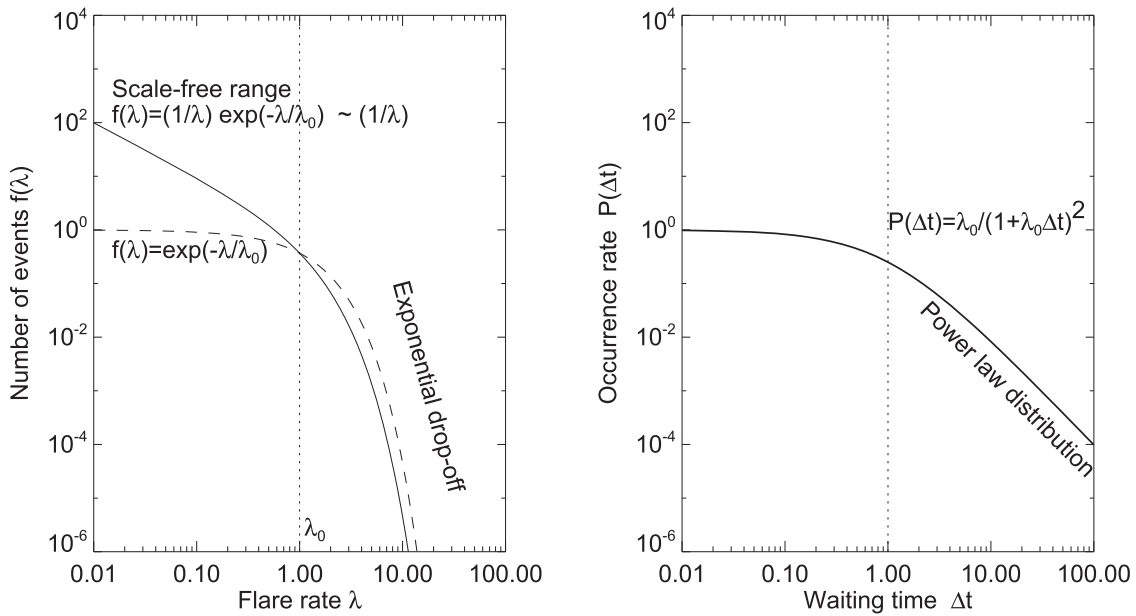


Figure 2. Left: the distribution function $f(\lambda)$ of the flaring rate is approximately reciprocal in the scale-free range $\lambda \lesssim \lambda_0$ and shows a steep exponential drop-off at larger flaring rates ($\lambda \gtrsim \lambda_0$). Right: the resulting waiting time distribution is predicted to have a power-law function $P(\Delta t) \propto \Delta t^{-2}$ at large waiting times $\Delta t \gtrsim \Delta t_0$, shown here for a value of $\lambda_0 = 1$.

$\int_0^\infty x e^{ax} dx = 1/a^2$ when integrated over $[0 < x < \infty]$, yielding the solution $p(\Delta t) = 1/(a^2 \lambda_0^2)$, and we obtain for the waiting time distribution,

$$p(\Delta t) = \frac{\lambda_0}{(1 + \lambda_0 \Delta t)^2}. \quad (8)$$

Note that this waiting time distribution contains no free variables, except for the normalization constant λ_0 . Thus, this model predicts universally a power-law slope of $\alpha_{\Delta t} = 2$ for any waiting time distribution. The only underlying assumption is the reciprocity of flaring rates and waiting times, which naturally emerges from the property of scale-freeness in SOC models (Aschwanden & McTiernan 2010).

A comparison of stationary and nonstationary waiting time distributions is shown in Figure 3, as well as for a slow-driven and fast-driven SOC model (Figure 3). Note the reciprocal relationship between the flare occurrence rate (y-axis in Figure 3) and the waiting time (x-axis in Figure 3), differing by a factor of 10^2 . A parametric set of theoretically predicted waiting times with various values of $\lambda_0 = 0.02, \dots, 0.12$ is shown in Figure 4(c).

2.2. Numerical Simulations of Waiting Time Distributions

It is customary to perform Monte Carlo simulations of waiting time distributions $N(\Delta t)d\Delta t$ or occurrence frequency distributions $N(x)dx$ by random generator values $x = x_1, x_2, \dots, x_n$ that have a prescribed function of their frequency distribution. Examples for exponential and power-law distributions are given in Section 7.1.4 of Aschwanden (2011a). The normalization is given by the integral of the probability function $p(x)$,

$$\int_0^\infty p(x) dx = 1. \quad (9)$$

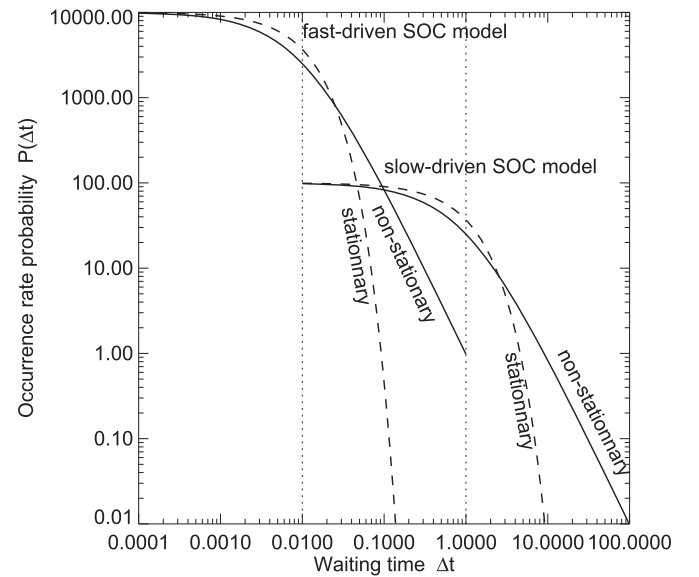


Figure 3. Overview of waiting time distributions for slow-driven and fast-driven, stationary and nonstationary SOC models.

The total probability $\rho(x)$ to have a value in the range of $[0, x]$ is then the integral

$$\rho(x) = \int_0^x p(x') dx'. \quad (10)$$

Then, we invert the integral function $\rho(x)$ and denote it by the analytical inverse function ρ^{-1} , so that

$$x = \rho^{-1}(\rho) = \rho^{-1}(\rho[x]), \quad (11)$$

yielding a transform that allows us to generate values x_i from a distribution of probability values ρ_i . There are many numerical random generator algorithms available that produce a random number ρ_i in a homogeneous range of $[0, 1]$, which can then be used to generate values x_i with the mapping transform

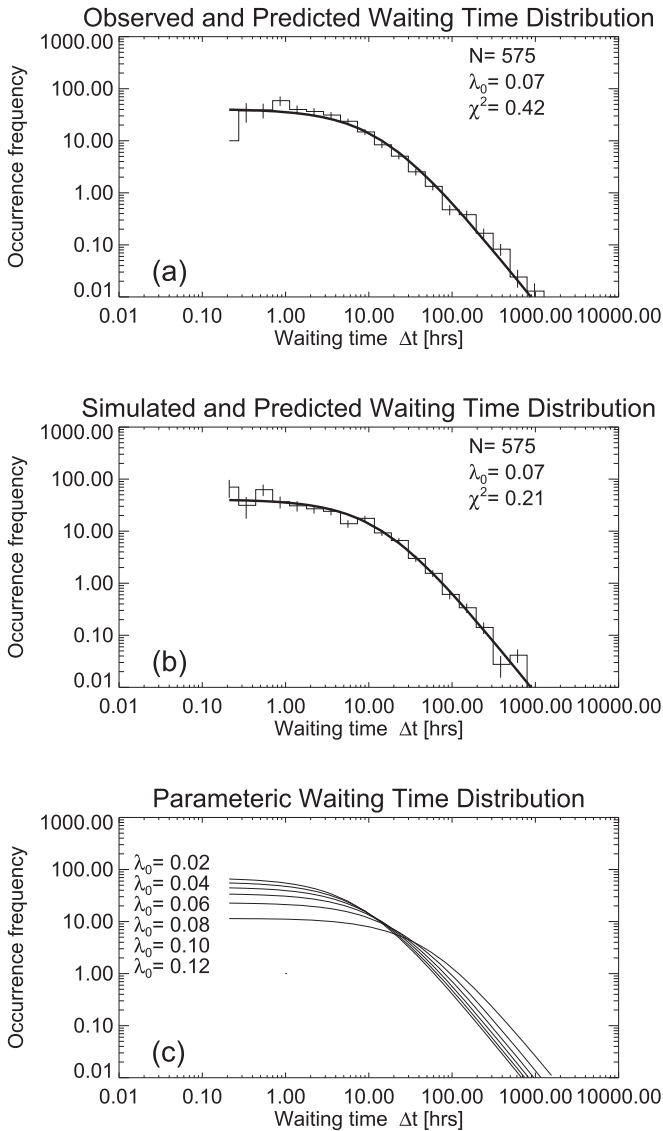


Figure 4. (a) Observed waiting time distribution of *GOES* M- and X-class flares (histogram) with predicted model (thick solid curve); (b) simulated waiting time distribution for the same normalization constant $\lambda_0 = 0.07$ (histogram) with predicted model (thick solid curve); and (c) parametric set of waiting time distributions for $\lambda_0 = 0.02, 0.04, \dots, 0.12 \text{ hr}^{-1}$.

$x_i = \rho^{-1}(\rho_i)$. The frequency distribution of these values x_i will then fulfill the prescribed function $p(x)$.

In our case, we want to simulate the waiting time distribution function that is given by the probability function $p(\Delta t)$ (Equation (8)),

$$p(\Delta t) = \frac{\lambda_0}{(1 + \lambda_0 \Delta t)^2}, \quad (12)$$

which fulfills the normalization

$$\int_0^1 p(\Delta t) d\Delta t = 1. \quad (13)$$

The integral function $\rho(\Delta t)$ of the probability function $p(\Delta t)$ is then

$$\rho(\Delta t) = \int_0^{\Delta t} \frac{\lambda_0}{(1 + \lambda_0 \Delta t')^2} d\Delta t' = \frac{\lambda_0 \Delta t}{1 + \lambda_0 \Delta t}. \quad (14)$$

The inversion of the probability function $\rho(\Delta t)$ is then simply

$$\Delta t = \frac{\rho}{\lambda_0(1 - \rho)}, \quad (15)$$

which can be used to simulate a set of waiting times Δt_i using random numbers ρ_i in the homogeneous range $[0, 1]$,

$$\Delta t_i = \frac{\rho_i}{\lambda_0(1 - \rho_i)}, \quad \text{for } [0 < \rho_i < 1]. \quad (16)$$

Such a simulation for $N = 575$ events and $\lambda_0 = 1.7$ is shown in Figure 4 (middle panel), along with the theoretical distribution function $p(\Delta t)$ (Equation (8)). An example of an observed waiting distribution function is shown in Figure 4(a), sampled from *Geostationary Operational Environmental Satellite (GOES)* M- and X-class flares (histogram in Figure 4(a)), which matches the predicted distribution (solid curve in Figure 4(a)) according to Equation (8) within the statistical uncertainties. A parametric set of the same type of waiting time distributions (Equation (8)) is shown in Figure 4(c), where the normalization constant λ_0 is varied.

3. Data Analysis

3.1. Observations and Data Selection

We analyzed the same data set of 170 solar flares presented in Aschwanden et al. (2014a), which includes all M- and X-class flares observed with the *SDO* (Pesnell et al. 2011) during the first 3.5 yr of the mission. This selection of events has a heliographic longitude range of $[-45^\circ, +45^\circ]$, for which magnetic field modeling can be facilitated without too severe foreshortening effects near the solar limb. We use the 45 s line-of-sight magnetograms from the HMI/*SDO* and make use of all coronal extreme-ultraviolet (EUV) channels of the Atmospheric Imaging Assembly (AIA)/*SDO* (in the six wavelengths 94, 131, 171, 193, 211, 335 Å), which are sensitive to strong iron lines (Fe VIII, IX, XII, XIV, XVI, XVIII, XXI, XXIV) in the temperature range of $T \approx 0.6\text{--}16$ MK. For most of the analysis, we analyzed images with a cadence of 6 minutes, but present one event with the full AIA time cadence of 12 s.

3.2. Magnetic Field Computations

The coronal magnetic field is modeled by using the line-of-sight magnetogram $B_z(x, y)$ from HMI/*SDO* and (automatically detected) projected loop coordinates $[x(s), y(s)]$ in each EUV wavelength of AIA. A full 3D magnetic field model $\mathbf{B}(x, y, z)$ is computed for each time interval and flare with a cadence of 6 minutes (0.1 hr). The total duration of a flare is defined by the *GOES* flare start and end times, including a margin of 0.5 hr before and after each flare. Such a margin (commensurable with the duration of the shortest flares; see Figure 8(d)) allows us to study the time evolution of a flare more comprehensively, because flare-related emission in soft X-rays often precedes the NOAA flare start time and extends past the NOAA flare end time.

The magnetic field is computed with the vertical-current approximation nonlinear force-free field (VCA-NLFFF) code, which is described for the original first version (Aschwanden 2013) and has been improved in accuracy in the second (Aschwanden et al. 2016b) and third (VCA3-NLFFF) versions (Aschwanden 2019b). Traditional nonlinear force-free field (NLFFF) codes have been found to produce large uncertainties

in the horizontal (transverse to the line-of-sight) magnetic field components (e.g., Wheatland et al. 2000; Wiegelmann 2004; Wiegelmann et al. 2006, 2012), mostly due to the fact that the force-free magnetic field is extrapolated from photospheric magnetograms, although the photosphere is not force free (Metcalf et al. 1995). Improvements have been attempted by preprocessing of the line-of-sight magnetograms by additional constraints that minimize the force-freeness and net torque balance (Wiegelmann et al. 2012), by applying a magnetohydrostatic model (Zhu et al. 2013; Wiegelmann et al. 2017; Zhu & Wiegelmann 2018) or different magnetic helicity computation methods (Thalmann et al. 2019). In contrast, our method of the Vertical-Current Approximation (VCA) NLFFF code circumvents this problem, because the magnetic modeling is constrained by coronal loop structures, which are believed to be force free in the low plasma-beta corona (although not during flares, but before and after flares).

3.3. Time Evolution of Free Energy

The main physical parameter that we are interested in here is the time evolution of the free energy, which is defined as the difference between the potential and nonpotential magnetic field, i.e., $E_{\text{free}}(t) = E_{\text{np}}(t) - E_p(t)$.

We show the time evolution of the free energy $E_{\text{free}}(t)$ for 20 flare events (out of the 170 analyzed events) in Figures 5–7. We decompose the time profiles into pulses that consist of a rise time phase $\tau_{\text{rise}} = t_p - t_s$ and a decay time phase $\tau_{\text{decay}} = t_e - t_p$. The peak times t_p are measured at the local maxima of the time evolution function $E_{\text{free}}(t)$, and the starting times t_s and end times are derived from the local minima preceding and following each peak time. For clarity, we represent the decay phases of the pulses with gray areas in Figures 5 and 6. In Figure 5, we show relatively simple flare events with one single peak ($n_p = 1$) or two peaks ($n_p = 2$), while the 10 cases shown in Figure 6 were selected from the flare events with the longest duration, which exhibit from $n_p = 5$ to $n_p = 13$ peaks.

In Figure 7, we show the time profiles of the free energy $E_{\text{free}}(t)$ with higher time resolution: the nominal resolution is 6 minutes (Figure 7(b)), an intermediate resolution is 1 minute (Figure 7(c)), and the full time resolution of AIA is 12 s (Figure 7(d)). The fluctuations visible at the highest cadence (Figure 7(d)) show a mean and standard deviation of $E_{\text{free}} = (42 \pm 7) \times 10^{30}$ erg, which indicates uncertainties of $\sigma_E \approx 7/42 \approx 0.17$. This uncertainty in the free energy includes numerical noise, mostly caused by the decomposition of unipolar magnetic charges from the HMI magnetograms and from the automated detection of coronal loops in the AIA images. Nevertheless, the time profiles shown in Figure 7 reveal about one to three significant pulses for this event, while Figure 6 shows 5–13 significant energy dissipation pulses per flare.

3.4. Statistics of Timescales

Statistics of timescales is given in Figure 8. The number of energy dissipation pulses per flare ranges from $n_p = 1$ to $n_p = 13$ (see Figures 5 and 6), as derived from the (slightly smoothed) time profiles of the free energy, $E_{\text{free}}(t)$. Each of the pulses is characterized by the rise time (which can be interpreted as magnetic energy loading time by new flux emergence), $\tau_{\text{rise}} = 0.1\text{--}1.2$ hr = 6–72 minutes (Figure 8(a));

the pulse decay time (which can be interpreted as magnetic energy dissipation time), $\tau_{\text{decay}} = 0.1\text{--}0.7$ hr = 6–42 minutes (Figure 8(b)); and the total pulse duration $\tau_{\text{pulse}} = 0.2\text{--}1.5$ hr = 12–90 minutes (Figure 8(c)). The lower limit of $\tau_{\text{rise,min}} = \tau_{\text{decay,min}} = 0.1$ hr = 6 minutes is caused by the chosen cadence in the calculation of magnetic energies.

The flare duration times have a range of $\tau_{\text{flare}} = 1.1\text{--}5.2$ hr (Figure 8(d)), which is about an order of magnitude longer than the pulse rise or decay times. This difference can be explained by the fact that the timescale of magnetic energy dissipation, which is similar to the duration of hard X-ray emission, is generally shorter than the timescale of soft X-ray emission, which was used by NOAA to define the flare duration.

Finally, we also measure the waiting times of flare events, using all GOES M- and X-class flare events during the first 3.5 yr of the SDO mission (from 2010 June 12 to 2014 November 16), including those events near the limb for which magnetic modeling was not feasible. The range of waiting times derived from the starting time difference of these 575 flares covers $\Delta t = 0.2\text{--}2000$ hr (Figure 8(e)). Note that truncation effects due to solar rotation and the selected longitudinal range ($\pm 45^\circ$) are ignored in the waiting time statistics here, although it could affect the correct waiting time measurement for events near the east or west limb. The waiting time distribution forms a power-law distribution with a slope of $\alpha_{\Delta t} = 2.0$ for timescales of $\Delta t \gtrsim 1$ hr (Figure 8(e)) and closely follows the predicted function derived theoretically (Equation (8)) for a normalization constant of $\lambda_0 = 0.07$ hr $^{-1}$. According to the definitions of waiting times Δt , energy storage times $\tau_{\text{storage}} \approx \tau_{\text{rise}}$, and energy dissipation times $\tau_{\text{diss}} \approx \tau_{\text{decay}}$ given in Figure 1, most of the storage times (Figure 8(a)) are much shorter than the waiting times (Figure 8(e)) and thus are consistent with the fast-driven SOC model (Figure 1(b)), rather than with the slow-driven SOC model (Figure 1(a)).

3.5. Correlation of Free Energy with Hard X-Rays

If the magnetic free energy is the main energy input in solar flares, and the energy converted into the acceleration of (nonthermal) particles E_{nth} conveys the major energy output, we would expect some correlation between the free energy time profile $E_{\text{free}}(t)$ and the hard X-ray flux time profile $F_{\text{HXR}}(t)$, which most easily can be inferred from the time derivative of the GOES soft X-ray time profile, i.e., $F_{\text{HXR}} = \partial F_{\text{HXR}}(t)/\partial t$, according to the Neupert effect (Neupert 1968; Dennis & Zarro 1993).

We juxtapose these two time profiles $E_{\text{diss}}(t)$ and $F_{\text{HXR}}(t)$ for 20 flare events in Figures 5 and 6, where the time profiles of the energy dissipation (inferred from the pulse decay time intervals marked with gray areas) and the GOES 1–8 Å flux (marked with hatched areas) are shown. While there are obvious correlations between the two time intervals in a number of single-pulse flares (e.g., event #53 in Figure 5(a), #187 in Figure 5(c)), in double-pulse flares (e.g., event #367 in Figure 5(i)), or in multipulse flares (e.g., event #54 in Figure 6(d), #150 in Figure 6(e)), we see also surprising cases where hard X-ray emission is detected for a single pulse only when a sequence of five magnetic energy pulses is present (e.g., event #171 in Figure 6(j), #219 in Figure 6(i)). Thus, we find both, well-correlated flare events as well as mismatching time profiles. This outcome of our study indicates that the simple-minded notion of magnetic energy dissipation with subsequent particle acceleration does not always fit the data.

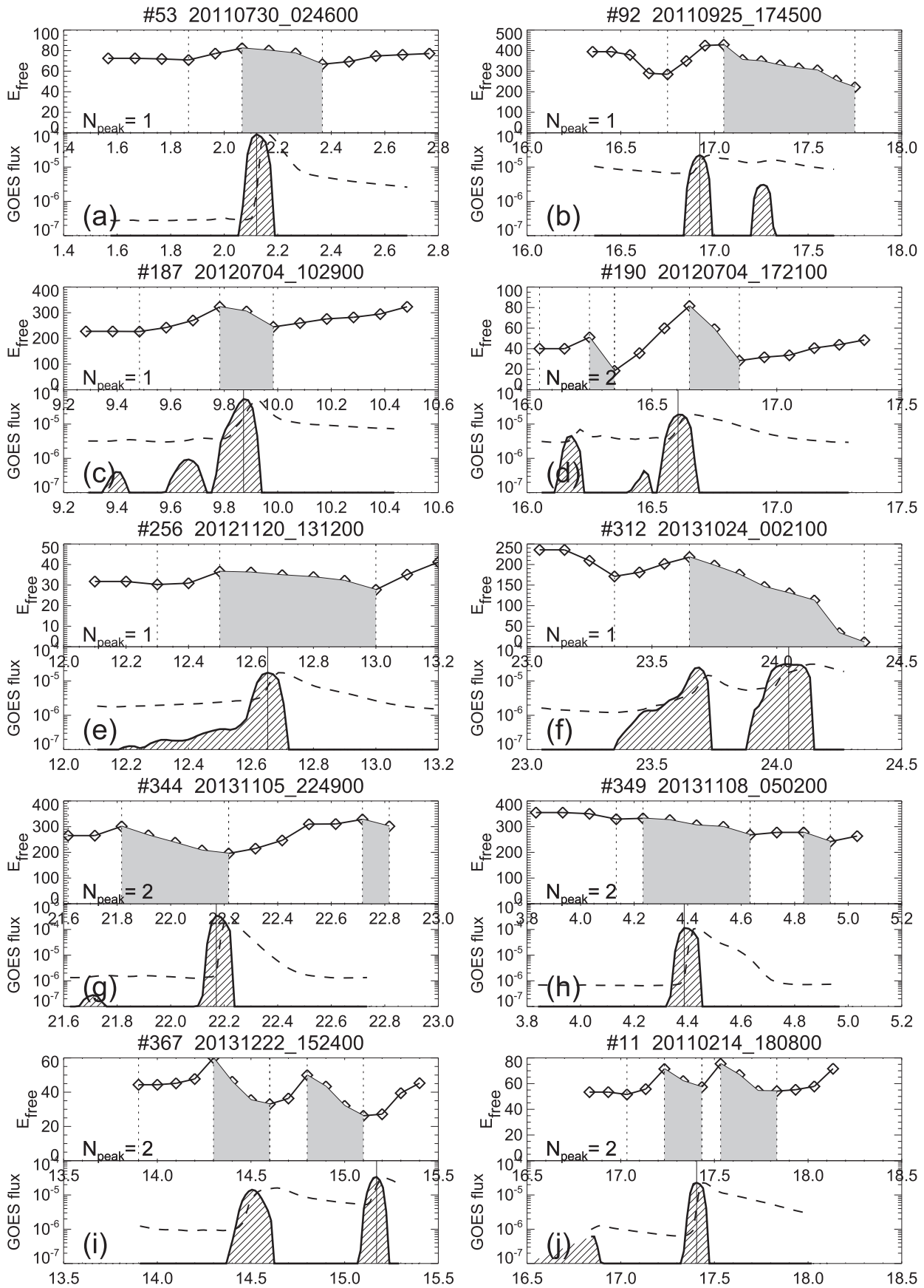


Figure 5. The time evolution of the free energy $E_{\text{free}}(t)$ in 10 flares with one or two peaks of the energy energy loading/dissipation episodes (thick black curves with diamonds). The GOES flux curve is indicated with a dashed curve, and the time derivative of the GOES curve with a solid line with hatched areas. The time intervals of energy dissipation are colored in gray.

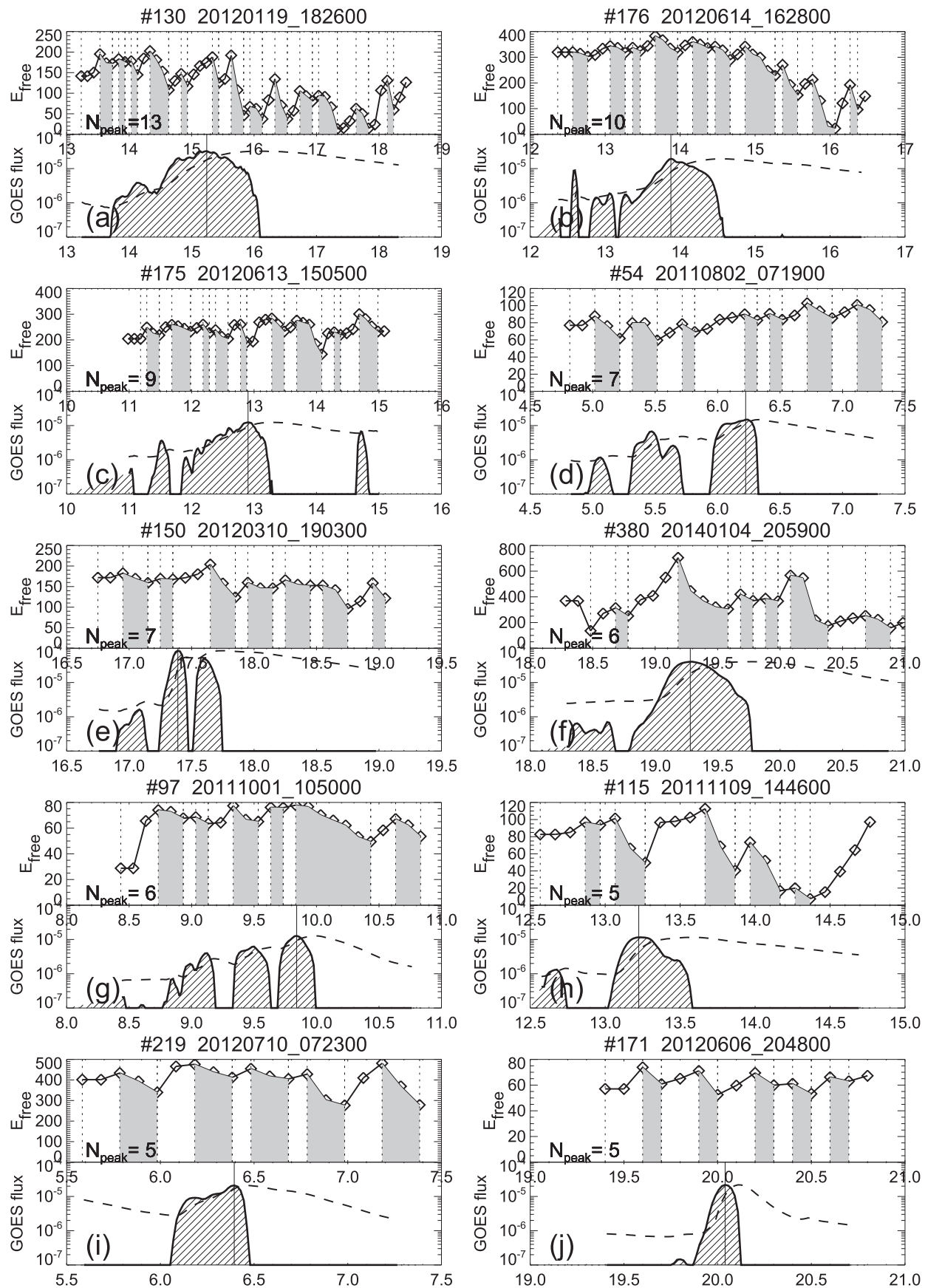


Figure 6. The time evolution of the free energy $E_{\text{free}}(t)$ in 10 flares with the largest number of energy loading/dissipation episodes ($N_{\text{peak}} = 5-13$; thick black curves with diamonds). The time intervals of energy dissipation are colored in gray; otherwise, similar presentation to Figure 5.

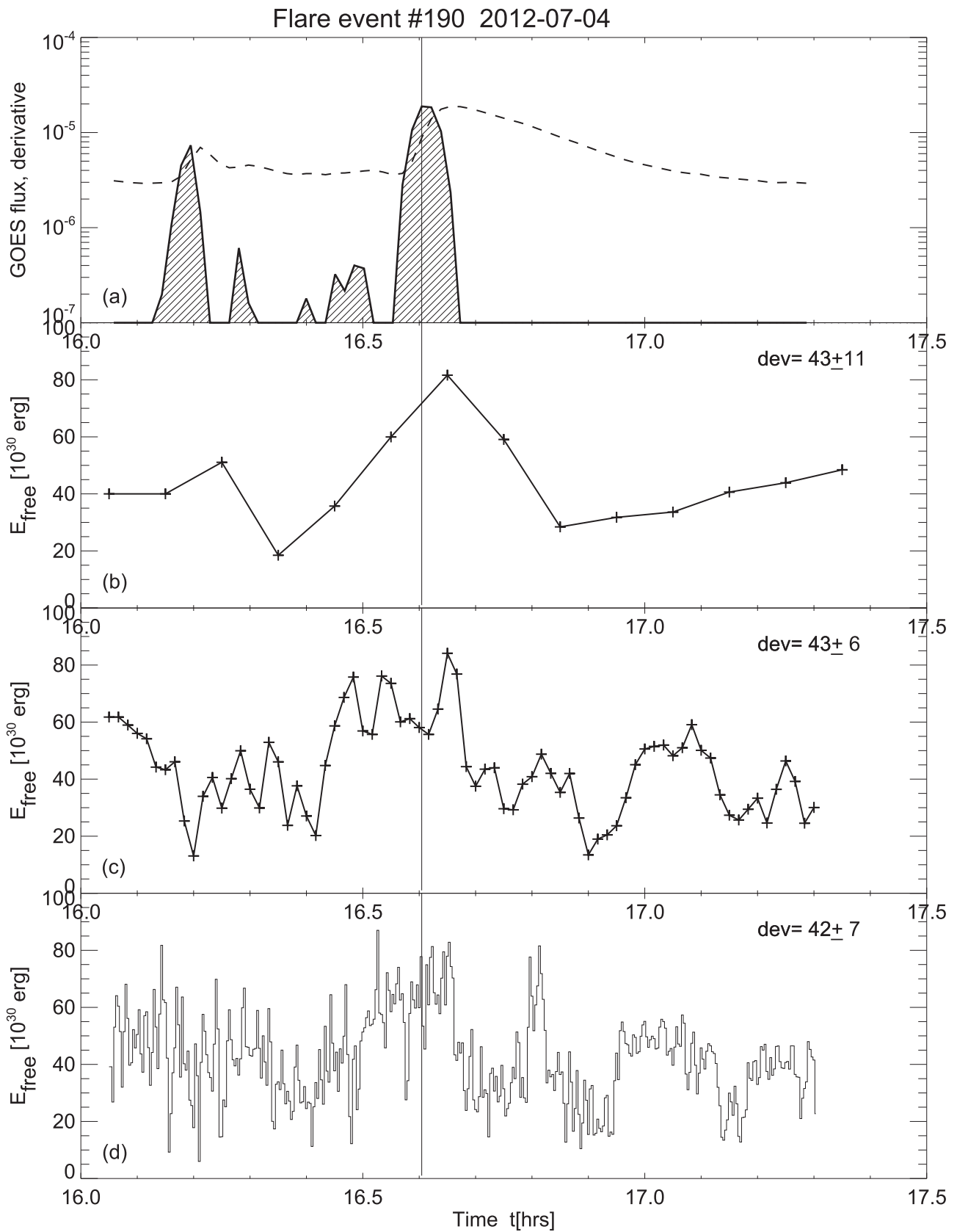


Figure 7. (a) GOES flux (dashed curve) and time derivative (hatched curve). The evolution of the free energy is shown with different time resolutions: (b) 6 minute cadence; (c) 1 minute cadence; (d) 12 s time cadence, where about three significant pulses are present (at 16.5–16.7, 16.8, and 16.95–17.15 UT).

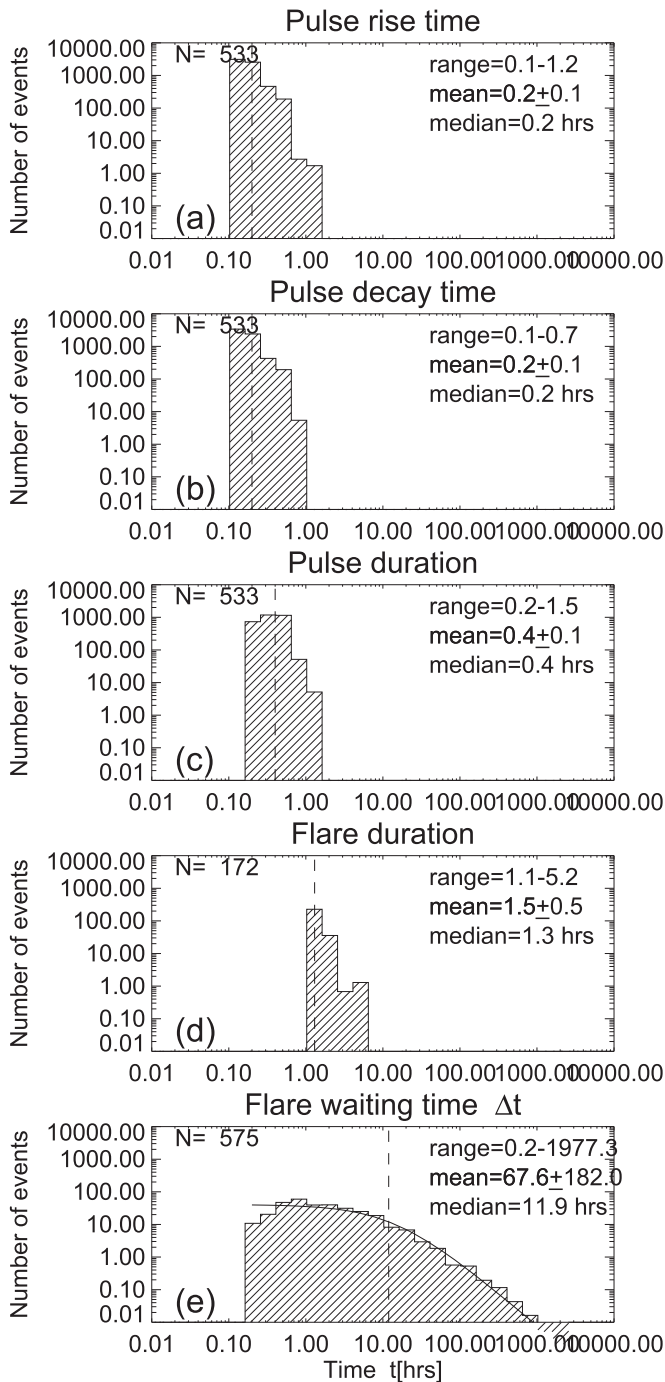


Figure 8. Number of events (per bin) as a function of (a) the free energy pulse rise time, (b) pulse decay time, (c) pulse durations, (d) flare duration, and flare waiting time distribution (bottom panel), along with the theoretical model for $\lambda_0 = 0.07$ (curve).

4. Discussion

4.1. Slow-driven SOC Models

We consider two different scenarios of the time evolution of energy dissipation in solar flares: the slow-driven self-organized criticality (SOC) model (Figure 1(a)) and the fast-driven SOC model (Figure 1(b)). The slow-driven SOC model corresponds to the model of cosmic transients proposed by Rosner & Vaiana (1978), while their time evolution can also be characterized by an exponential-growth model, a power-law

growth model, or a logistic-growth model (Section 3 of Aschwanden 2011a). Besides the application to solar flare observations, slow external driving of photospheric motion is expected to lead to occasional relaxation events also, at random times, with random amplitudes (Longcope & Sudan 1992). The essential property of the slow SOC model is the exponential growth of energy build-up during the time interval between two subsequent flare events, which eventually creates a flare at a random time interval, and then relaxes into a more stable state than before. The exponential-growth function, together with Poissonian random statistics, leads to the prediction of a power-law function of the flare size distribution (Rosner & Vaiana 1978). Moreover, the monotonic growth of the free energy predicts a correlation between the flare size and the interflare (waiting) time interval. However, observational searches for such a correlation between the flare sizes and flare waiting times turned out to be negative (Lu 1995; Crosby et al. 1998; Wheatland 2000a; Moon et al. 2001; Lippello et al. 2010). The only correlation found was that smaller active regions produce smaller flare sizes (Wheatland 2000b) and that small active regions produce deviations from power laws (Wheatland 2010). There are also the problems that large flares sometimes occur within shorter waiting times than the required energy build-up times of the Rosner–Vaiana model: sometimes a larger flare volume than available is required, or too many e-folding growth times are necessary (Lu 1995). Nevertheless, a correlation of the flare size with the time interval after a flare (rather than before) was claimed for a small sample of flare events in the same active region (Hudson 2019). In summary, none of the predictions of the slow-driven SOC model of Rosner & Vaiana (1978) could be confirmed by solar flare observations.

4.2. Fast-driven SOC Models

Most of the simulations of the (frequency occurrence) size distributions of SOC avalanches assume a separation of timescales, which means that the avalanche duration τ_{flare} or energy dissipation timescale τ_{diss} is much shorter than the waiting time between two subsequent avalanches, i.e., $\tau_{\text{flare}} \ll \Delta t_{\text{wait}}$. If the input rate (e.g., of sand grains dripped on a sandpile) is sufficiently slow, the statistical properties of avalanche sizes and durations are expected not to change (Pruessner 2012). However, the observed statistics of solar flares was found to violate the timescale separation during the solar cycle maximum era (Aschwanden 2011a, 2011b, 2011c; Aschwanden & Freeland 2012), when the flare duration exceeded the waiting times, i.e., $\tau_{\text{flare}} \gtrsim \Delta t_{\text{wait}}$, which we call a fast-driven SOC system. Because the mean waiting time $\langle \Delta t_{\text{wait}} \rangle$ is defined by the total duration T of the observations, divided by the total number N_{ev} of events (or intervals),

$$\langle \Delta t_{\text{wait}} \rangle = \frac{T}{N_{\text{ev}}}, \quad (17)$$

the mean waiting time decreases reciprocally with the number of events, and thus becomes shorter for a faster input rate, as shown in Figure 3 for a fast driver that has a factor of 10^2 higher event number, but also a factor of 10^2 shorter mean waiting time. As the 10 examples in Figure 6 demonstrate, a number of $N_{\text{peak}} = 5\text{--}13$ flare peaks occur in large flares, which represent elementary flare substructures (Aschwanden et al. 1998) that we interpret as individual energy dissipation

events in a fast-driven SOC system. Thus, we detect rapid fluctuations of the free energy $E_{\text{free}}(t)$ before, during, and after large flares in a fast-driven SOC system (Figures 5 and 6), but the free energy does not monotonically increase between two subsequent flares (Figure 1(a)). Hence, the fast-driven SOC model (Figure 1(b)) is more consistent with the observations than the slow-driven SOC model (Figure 1(a)).

4.3. The Time Evolution of the Free Energy

If the free (magnetic) energy that is dissipated during a solar flare would all be stored in the corona, we should see a negatively dropping step function of the free energy $E_{\text{free}}(t)$ during the flare duration (Figure 1(a)). One of the most detailed studies on the time evolution of the free energy shows a gradual build-up of free energy over two days, culminating with an X2.2 GOES-class flare and a simultaneous downward step in the free energy (Sun et al. 2012; Aschwanden et al. 2014b). However, discrepancies up to a factor of $\lesssim 10$ have been noticed in the decrease of free energy during flares, when the standard Wiegmann-NLFFF code (with preprocessing) was employed in addition to our VCA-NLFFF code (Aschwanden et al. 2014b), which was reduced down to a factor of $\lesssim 3$ in recent refined magnetic modeling (Aschwanden 2019b). Besides the expected step functions, we also observe in the present study a number of pulses in the free energy that have a short rise time and decay time, on the order of $\tau_{\text{rise}} \approx \tau_{\text{decay}} \approx \tau_{\text{pulse}}/2 \approx 0.2 \pm 0.1 \text{ hr} = 12 \pm 6 \text{ minutes}$ (Figures 8(a), (b), (c)).

A puzzling question is what mechanism causes the relatively short rise time of the free energy? One mechanism that we know produces an increase of the free energy is the helical twisting by vertical currents (as it is incorporated in the VCA-NLFFF code used here), but then the twisting with subsequent untwisting produces a time-symmetric pulse in the free energy without a net energy transfer. Another possible mechanism is the coronal illumination effect, where the twisted loops are not visible in the initial flare phase, but become detectable when chromospheric evaporation starts to fill up the flare loops (Aschwanden et al. 2014a). A third possibility is chromospheric energy injection into the corona produced by energy transferred from the turbulent convection zone and photosphere into the corona, e.g., via anomalous current dissipation (Rosner et al. 1978). Such a scenario, with the ultimate energy source in the convection zone rather than in the corona, can draw large amounts of free energy to generate a flare without requiring coronal storage. Magneto-convection as seen in photospheric granulation cells has typical spatial scales of $\approx 1000 \text{ km}$ and turnover times of $\approx 7 \text{ minutes}$, which produces new emerging flux on timescales close to the observed pulse rise times of $\tau_{\text{pulse}} \approx 12 \pm 6 \text{ minutes}$ (Figure 8(a)). In conclusion, the time evolution of the free energy $E_{\text{free}}(t)$ provides crucial constraints on how and where the flare energy is stored.

4.4. Nonstationary Driver and Waiting Time

From the waiting time distribution, we can learn whether an SOC system is stationary or nonstationary, which means whether or not the mean flaring rate is constant, as a function of time. In the original SOC concepts of Bak et al. (1987), it was assumed that individual avalanches are statistically independent events, and thus the waiting time distribution should form a Poissonian (or exponential) distribution function. If there is a deviation from

a Poissonian distribution apparent, individual avalanche events could not be independent events, such as in sympathetic flares (Moon et al. 2002, 2003; Wheatland 2002, 2006; Wheatland & Craig 2006). However, when the flaring rate is not constant, the resulting waiting time distribution can be calculated by summing the partial waiting time distributions for each flaring rate (Wheatland et al. 1998; Wheatland & Glukhov 1998; Wheatland 2000c) as we summarize in Section 2 of this paper (and in Section 5 of Aschwanden 2011a). Waiting time distributions of solar flare data generally show a power-law distribution with a slope of $\alpha_{\Delta t} \approx 2-3$, (Wheatland et al. 1998; Moon et al. 2001; Wheatland 2003; Aschwanden & McTiernan 2010; Kanazir & Wheatland 2010), which is explained here with a model that is based on the universal reciprocal relationship between the (time-varying) mean flaring rate and the (time-varying) waiting time, and predicts a slope of $\alpha_{\Delta t} = 2$. In summary, the nonstationary Poissonian model provides the most natural explanation for the observed power-law-like waiting time distributions.

Besides the nonstationary Poissonian model of a fast-driven SOC model, some alternative interpretations have been explored, too, by other studies in the literature. An energy balance model in terms of a master equation between energy build-up and energy loss by dissipation of free energy has been proposed (Wheatland & Glukhov 1998; Wheatland & Litvinenko 2001, 2002; Wheatland 2008, 2009, 2009). Other approaches use scaling laws from magnetic reconnection processes (Litvinenko 1996; Wheatland & Craig 2003, 2006). Alternative functions for waiting time distributions were also tested, finding that lognormal and inverse Gaussian distribution functions are more likely to fit the observations than the exponential function (Kubo 2008).

5. Conclusions

Standard SOC models, mostly inspired by the paradigm of sandpile avalanches introduced by Bak et al. (1987), assume a slow-driven energy dissipation system, a stationary energy input rate, a fixed (critical) threshold for triggering of avalanches, timescale separation between avalanche time durations τ_{dur} and inter-event waiting times Δt , i.e., $\tau_{\text{dur}} \gg \Delta t$, and statistical independence of individual avalanche events. These assumptions predict power-law distribution functions for most avalanche parameters (such as the size and duration) and exponential distributions for the waiting times. In reality, however, most of these assumptions are violated, but it appears that SOC models are sufficiently robust to preserve some power-law characteristics, even in the presence of violated assumptions. In this study, we explore nonstandard SOC models that account for the violated assumptions, in particular for the phenomenon of solar flares. Our findings are the following:

1. The waiting time distribution: one not understood problem is the functional shape of the waiting time distribution, because the assumption of statistical independence of individual avalanche events predicts an exponential function, while the observations exhibit a power-law distribution with a slope of $\alpha_{\Delta t} \approx 2-3$. One possible solution of this problem is the nonstationary Poisson model, introduced by Wheatland & Litvinenko (2002), but the functional shape of the flaring rate $\lambda(t)$ has not been constrained. The shape of observed

waiting time distributions has been reconciled empirically with the near-reciprocal flaring rate function $f(\lambda) = \lambda^{-1} \exp(-\lambda/\lambda_0)$ (Equation (6)) in the previous study of Aschwanden & McTiernan (2010). In the present study, we provide a physical reason in terms of the universally valid reciprocal relationship between the mean flaring rate $\langle \lambda \rangle$ and the mean waiting time $\langle \Delta t \rangle$, i.e., $f(\lambda) \propto \langle \lambda \rangle^{-1} = \langle \Delta t \rangle$. The reciprocal relationship predicts then a power-law distribution for the waiting time distribution, with a power-law slope of $\alpha_{\Delta t} = 2$, without any free parameters, except for a normalization constant λ_0 .

2. Nonstationarity of the SOC model: the power-law shape of the waiting time distribution thus yields a sufficient (but not necessary) condition for the nonstationarity of the flare rate that drives the generation of solar flares. The flare rate varies up to two orders of magnitude between the minimum or maximum of the solar magnetic (Hale) cycle. There are also large variations in the flaring rate on shorter timescales, down to weeks, days, or hours. All this variability produces power-law-like distributions of waiting times. Moreover, it also produces power-law distributions for the sizes and durations of flares, which appears to be a very robust feature of SOC models, regardless of whether the driver is stationary or nonstationary.
3. Slow-driven and fast-driven SOC models: while the duration of an avalanche (e.g., a solar flare) is much shorter than the waiting time between two subsequent avalanche events in standard SOC models, we find that this behavior is only true in quiescent periods during the solar cycle minimum, especially when the SOC threshold is high and the flaring rate is low. However, the flare rate during solar maximum conditions is often so high that near-simultaneous flare events overlap in time, and thus the flare duration becomes comparable with the waiting time or even exceeds the waiting time. The solar dynamo thus produces an SOC system that oscillates between slow-driven and fast-driven operation cycles.
4. The Rosner & Vaiana (1978) model: this model predicts a continuously growing energy storage between two flare events and thus a correlation between the waiting time and dissipated energy during the following event. Observations do not confirm that energy is stored between two flares, nor is there any correlation between storage time and energy dissipation. Although we can measure free (magnetic) energy before, during, and after flares, we rarely see a simple step function of the free energy that drops from a high preflare level to a low postflare level.
5. Pulsed free energy dissipation: instead of a step function in the time evolution of the free energy, we observe that the free energy exhibits pulses with rise times and decay times of $\approx 12 \pm 6$ minutes, which occur between 1 and 13 times during a flare, depending on the flare duration (1.1–5.2 hr). The fact that each pulse exhibits a fast rise (rather than a slow rise as expected in storage models) indicates that free energy is intermittently generated (rather than stored over long time intervals), for instance by photospheric convection, which shows similar turn-over times of order ≈ 7 minutes in the photospheric granulation layer.

Based on these results, we recommend modifying numerical simulations of SOC models with the following features, in order to obtain a more realistic representation of solar flare data: (i) a nonstationary driver that varies from slow-driven dynamics during the solar minimum to fast-driven dynamics during the solar maximum; (ii) separate fitting of time periods with low and high flaring rates, possibly measuring the flaring rate distribution $\lambda(t)$ as a function of time; (iii) fitting of the predicted waiting time distribution model $p(\Delta t) = \lambda_0/(1 + \lambda_0\Delta t)^2$ (rather than fitting a straight power-law function); (iv) localization of photospheric convection vortices during flares in magnetogram data that contribute most significantly to local increases in the free energy during flares; and (v) spatiotemporal disentangling of near-simultaneous flare sites during fast-driven time periods.

Part of the work was supported by NASA contract NNG 04EA00C of the *SDO/AIA* instrument and the NASA *STEREO* mission under NRL contract N00173-02-C-2035.

ORCID iDs

Markus J. Aschwanden  <https://orcid.org/0000-0003-0260-2673>

References

- Aschwanden, M. J. 2011a, *Self-Organized Criticality in Astrophysics. The Statistics of Nonlinear Processes in the Universe* (New York: Springer-Praxis)
- Aschwanden, M. J. 2011b, *SoPh*, **274**, 99
- Aschwanden, M. J. 2011c, *SoPh*, **274**, 119
- Aschwanden, M. J. 2013, *SoPh*, **287**, 323
- Aschwanden, M. J. 2016b, *ApJS*, **224**, 25
- Aschwanden, M. J. 2019a, *New Millennium Solar Physics*, *Astrophysics and Space Science Library*, Vol. 458 (Cham: Springer)
- Aschwanden, M. J. 2019b, *ApJ*, **885**, 49
- Aschwanden, M. J., Crosby, N., Dimitropoulou, M., et al. 2016a, *SSRv*, **198**, 47
- Aschwanden, M. J., Dennis, B. R., & Benz, A. O. 1998, *ApJ*, **497**, 972
- Aschwanden, M. J., & Freeland, S. L. 2012, *ApJ*, **754**, 112
- Aschwanden, M. J., & McTiernan, J. M. 2010, *ApJ*, **717**, 683
- Aschwanden, M. J., Xu, Y., & Jing, J. 2014a, *ApJ*, **797**, 50
- Aschwanden, M. J., Xu, Y., & Liu, Y. 2014b, *ApJ*, **785**, 34
- Bak, P., Tang, C., & Wiesenfeld, K. 1987, *PhRvL*, **59/4**, 381
- Charbonneau, P. 2013, in *Self-Organized Criticality Systems*, ed. M. J. Aschwanden (Berlin: Open Academic Press), 371
- Charbonneau, P., McIntosh, S. W., Liu, H. L., & Bogdan, T. J. 2001, *SoPh*, **203**, 321
- Crosby, N., Vilmer, N., Lund, N., & Sunjaev, R. 1998, *A&A*, **334**, 299
- Crosby, N. B., Aschwanden, M. J., & Dennis, B. R. 1993, *SoPh*, **143**, 275
- Dennis, B. R., & Zarro, D. M. 1993, *SoPh*, **146**, 177
- Hudson, H. S. 2019, *MNRAS*, submitted
- Jaynes, E. T. 2003, *Probability Theory: The Logic of Science* (Cambridge: Cambridge Univ. Press), 758
- Kanazir, M., & Wheatland, M. S. 2010, *SoPh*, **266**, 301
- Kubo, Y. 2008, *SoPh*, **248**, 85
- Lippiello, E., de Arcangelis, L., & Godano, C. 2010, *A&A*, **511**, L2
- Litvinenko, Y. E. 1996, *SoPh*, **167**, 321
- Litvinenko, Y. E., & Wheatland, M. S. 2001, *ApJL*, **550**, L109
- Longcope, D. W., & Sudan, R. N. 1992, *PhFIB*, **4**, 2277
- Lu, E. T. 1995, *ApJ*, **447**, 416
- Lu, E. T., & Hamilton, R. J. 1991, *ApJL*, **380**, L89
- Metcalf, T. R., Jiao, L., Uitenbroek, H., McClymont, A. N., & Canfield, R. C. 1995, *ApJ*, **439**, 474
- Moon, Y. J., Choe, G. S., Park, Y. D., et al. 2002, *ApJ*, **574**, 434
- Moon, Y. J., Choe, G. S., Wang, H., & Park, Y. D. 2003, *ApJ*, **588**, 1176
- Moon, Y. J., Choe, G. S., Yun, H. S., & Park, Y. D. 2001, *JGR*, **106/A12**, 29951
- Neupert, W. M. 1968, *ApJL*, **153**, L59
- Pesnell, W. D., Thompson, B. J., & Chamberlin, P. C. 2011, *SoPh*, **275**, 3

- Pruessner, G. 2012, *Self-organised Criticality. Theory, Models and Characterisation* (Cambridge: Cambridge Univ. Press)
- Rosner, R., Golub, L., Coppi, B., & Vaiana, G. S. 1978, *ApJ*, 220, 643
- Rosner, R., & Vaiana, G. S. 1978, *ApJ*, 222, 1104
- Scargle, J. 1998, *ApJ*, 504, 405
- Sivia, D. S., & Skilling, J. (ed.) 2006, *Data Analysis—A Bayesian Tutorial* (2nd ed.; Oxford: Oxford Univ. Press), 264
- Sun, X., Hoeksema, J. T., Liu, Y., et al. 2012, *ApJ*, 748, 77
- Thalmann, J. K., Linan, L., Pariat, E., & Valori, G. 2019, *ApJL*, 880, L6
- Wheatland, M. S. 2000, *ApJ*, 532, 1209
- Wheatland, M. S. 2000a, *ApJ*, 532, 1209
- Wheatland, M. S. 2000b, *SoPh*, 191, 381
- Wheatland, M. S. 2000c, *ApJL*, 536, L109
- Wheatland, M. S. 2002, *SoPh*, 208, 33
- Wheatland, M. S. 2003, *SoPh*, 214, 361
- Wheatland, M. S. 2006, *SoPh*, 236, 313
- Wheatland, M. S. 2008, *ApJ*, 679, 1621
- Wheatland, M. S. 2009, *SoPh*, 255, 211
- Wheatland, M. S. 2010, *ApJ*, 710, 1324
- Wheatland, M. S., & Craig, I. J. D. 2003, *ApJ*, 595, 458
- Wheatland, M. S., & Craig, I. J. D. 2006, *SoPh*, 238, 73
- Wheatland, M. S., & Glukhov, S. 1998, *ApJ*, 494, 858
- Wheatland, M. S., & Litvinenko, Y. E. 2001, *ApJ*, 557, 332
- Wheatland, M. S., & Litvinenko, Y. E. 2002, *SoPh*, 211, 255
- Wheatland, M. S., Sturrock, P. A., & McTiernan, J. M. 1998, *ApJ*, 509, 448
- Wheatland, M. S., Sturrock, P. A., & Roumeliotis, G. 2000, *ApJ*, 540, 1150
- Wiegelmann, T. 2004, *SoPh*, 219, 87
- Wiegelmann, T., Inhester, B., & Sakurai, T. 2006, *SoPh*, 233, 215
- Wiegelmann, T., Neukirch, T., Nickeler, D. H., et al. 2017, *ApJ*, SS229, 18
- Wiegelmann, T., Thalmann, J. K., Inhester, B., et al. 2012, *SoPh*, 281, 37
- Zhu, X. S., Wang, H. N., Du, Z. L., et al. 2013, *ApJ*, 768, 119
- Zhu, X. S., & Wiegelmann, T. 2018, *ApJ*, 866, 130